# Crystallinity of nano C-LiFePO$_4$ prepared by the polyol process

T. Azib [a], S. Ammar [a], S. Nowak [a], S. Lau-Truing [a], H. Groult [b], K. Zaghib [c,*], A. Mauger [d], C.M. Julien [b]

[a] ITODYS, Université Paris Diderot, UMR7086, 15, rue Jean-Antoine de Baïf, 75205 Paris, France
[b] Université Pierre et Marie Curie-Paris6, PECSA, UMR7195, 4 place Jussieu, 75005 Paris, France
[c] Institut de Recherche d'Hydro-Quebec, 1800 Bd Lionel-Boulet, Varennes, QC, Canada J3X1S1
[d] Université Pierre et Marie Curie-Paris6, IMPMC, UMR7590, 2–4 place Jussieu, 75005 Paris, France

## HIGHLIGHTS

► Polyol-made LiFePO$_4$/Cgr nanocrystals were evaluated as cathode for Li$^+$-batteries.
► The role of antisite defects and the coherence length along the b-axis was emphasized.
► A capacity of 151 mAh g$^{-1}$ at low C-rate was reached

## ARTICLE INFO

## ABSTRACT

Size and shape-tuned LiFePO$_4$ nano-platelets were prepared by the polyol process to examine the effect of their microstructure on their electrochemical performance when coated by a thin carbon layer. The materials were characterized by X-ray diffraction, scanning and transmission electron microscopy, magnetic susceptibility, Fourier transform infrared and Raman spectroscopy. The crystallinity, as well as the size of the particles, depends on the nature of the solvent that is used, and also on the rate of dilution. The electrochemical properties emphasize the role of antisite defects and the coherence length along the b-axis, i.e. along the Li channels. With an optimized choice of the synthesis parameters, the results showed that the orthorhombic olivine structure is retained even in crystals of few nanometers in width, a free of impurities. The high crystalline quality of the particles obtained in these optimized conditions lead to a good electrochemical performance of the nanocomposite C-LiFePO$_4$ product as a cathode material for lithium-ion batteries, with a capacity 151 mAh g$^{-1}$ at low C-rate, despite the presence of residual adsorbed polyol species that are found to be insulating.

© 2012 Elsevier B.V. All rights reserved.

## 1. Introduction

Electric energy storage demands for portable electronic devices and electrical vehicles are ever growing, and the production of advanced electrode materials for lithium ion batteries exhibiting higher energy and power densities remains critical. Olivine structured LiFePO$_4$ has attracted much interest as positive electrode due to its low cost, low toxicity, flat discharge-charge potential at 3.45 V vs. Li/Li$^+$ owing to Fe$^{2+}$/Fe$^{3+}$ redox couple, and high theoretical capacity ($\sim$ 170 mAh g$^{-1}$) [1]. However, this material suffers from a small electronic conductivity ($10^{-9}$–$10^{-10}$ S cm$^{-1}$) and slow kinetics of lithium ion diffusion ($D_{Li+} = 10^{-14}$ cm$^2$ s$^{-1}$) at room temperature [2,3], which may result in a loss of capacity during high rate discharge. Over the past decades, many efforts have been

devoted to overcome these drawbacks. Coating with an electron-conducting layer, mostly conductive carbon [4], and particle size reduction have solved the problem of the poor ionic and electronic transport. The mean path of the electrons inside LiFePO$_4$ is reduced to the size of the particle, before it is driven to the aluminum collector by the conductive carbon that percolates through the powder. However, the decrease of the size down to few tens of nanometers may also affect the structural properties, since the surface effects become critical. It is then suspected that such small sizes favour impurities and defects, amorphization, in summary effects that decrease the electrochemical performance (for a review on surface effects, see Ref. [5]), although some well-crystallized 20 nm LiFePO$_4$ particles of LiFePO$_4$ could be obtained [6]. The control of the purity and crystallinity of small particles is thus currently an important challenge.

The control of the shape of the LiFePO$_4$ crystallites is also a key parameter, because computational and experimental studies indicate that Li$^+$ ion migration occurs preferentially via one-

* Corresponding author. Tel.: +1 4506528019; fax: +1 4506528424.
E-mail addresses: zaghib.karim@ireq.ca, zaghib.karim@ireq.ca (K. Zaghib).

dimensional channels oriented along the (010) direction of the orthorhombic crystal structure, so that the ionic diffusivity is highly anisotropic [7–9]. Therefore, replacing LiFePO$_4$ spherical sub-micrometric particles by ultrathin platelets with basal faces perpendicular to the (010)-axis should provide both high power and very long cycling life. In particular, Richardson et al. suggested that the use of thin, non-agglomerated particles with large (010) surface area would increase the active area and decrease the diffusion distances for Li ions [10].

In the present work, we produce size- and shape-controlled LiFePO$_4$ nano-platelets that are highly crystallized using a well-known soft chemistry synthesis process, the polyol process [11–14]. We succeeded in decreasing the thickness of these particles down to 10 nm, without opposing their crystallinity. These nanoparticles were subsequently coated with conductive carbon. The electrochemical properties of the resulting composite nano-structures tested in lithium cell give evidence of the important role of the microstructure of the LiFePO$_4$ nanoparticles. The main results are discussed, underlying the role of the crystallinity and adsorb residual polyol species on the electrochemical behaviour of the produced C-LiFePO$_4$ nanocomposites.

## 2. Experiments

### 2.1. Chemicals

All chemicals were of analytical grade and used without further purification. Fe(CH$_3$CO$_2$)$_2$ and Li(CH$_3$CO$_2$)$_2 \cdot$2H$_2$O metal acetate salts were purchased from Acros and Fluka respectively; H$_3$PO$_4$ phosphoric acid from Prolabo, HO(CH$_2$)$_2$O(CH$_2$)$_2$OH diethyleneglycol (abbreviated as DEG hereafter), HO(CH$_2$)$_2$O(CH$_2$)$_2$O(CH$_2$)$_2$OH triethyleneglycol (tEG) and HO(CH$_2$)$_2$O(CH$_2$)$_2$O(CH$_2$)$_2$O(CH$_2$)$_2$OH tetraethyleneglycol (TEG) from Acros.

### 2.2. Particle synthesis

LiFePO$_4$ nanoparticles were synthesized using the polyol process. Typically, iron (3 g) and lithium (1.7 g) salts were mixed with the phosphoric acid (1.153 mL) in 1 L of polyol. The mixture was mechanically stirred while heated up to reflux (6 °C min$^{-1}$) and maintained at ebullition for 4 h. The reaction medium was then cooled down to room temperature. A green powder was recovered by centrifugation, washed 3 times with ethanol and dried in air at 50 °C. Three polyol solvents were tested: DEG, tEG and TEG. The 3 g iron salt in the solution reported above corresponds to a concentration (1.72 ± 0.02) × 10$^{-2}$ mol L$^{-1}$ of the iron precursor. A second set of samples was also prepared with a concentration 10 times smaller (0.172 ± 0.002) × 10$^{-2}$ mol L$^{-1}$ (see Table 1).

### 2.3. Carbon coating

The as-produced particles were mixed with lactose as carbon source and heated at 700 °C for 1 h under argon atmosphere,

**Table 1**
Main structural data of the LiFePO$_4$ particles. The particles are named a–d depending on the nature of the polyol solvent and the iron salt concentration. The polyol sovents are triethyleneglycol (tEG) and tetraethyleneglycol (TEG). The two iron salt concentrations labeled S (small) and L (large) are 0.172 × 10$^{-2}$ and 1.72 × 10$^{-2}$ mol L$^{-1}$, respectively (see Section 2.1).

| Sample | [Fe salt] | Solvent | $T_{boiling}$, °C | $a$, Å | $b$, Å | $c$, Å | $V$ (Å$^3$) |
|---|---|---|---|---|---|---|---|
| (a) | (L) | TEG | 325 | 10.3157(4) | 6.0011(2) | 4.6987(2) | 290.87(3) |
| (b) | (S) | | | 10.3030(3) | 6.0034(2) | 4.7025(2) | 290.86(3) |
| (c) | (L) | tEG | 285 | 10.3140(6) | 5.9971(3) | 4.7070(3) | 291.15(5) |
| (d) | (S) | | | 10.2803(4) | 5.9944(3) | 4.7059(2) | 290.00(4) |

following the process described elsewhere to obtain particles covered with a homogeneous 3-nm thick carbon layer [5].

### 2.4. Particles characterization

The X-ray diffraction (XRD) patterns of the powders were recorded with a PANalytical X'Pert Pro diffractometer equipped with a multichannel X'celerator detector and a Co X-ray tube ($\lambda = 1.7889$ Å) in the 10–70° 2$\theta$ range with a scan step of 0.016°. The cell parameter and the size of coherent diffraction domain (crystal size) were determined with the MAUD-Materials Analysis Using Diffraction software [15], which is based on the Rietveld method combined with Fourier analysis, well-adapted for broadened diffraction peaks. Polycrystalline strain-free silicon was used as standard to quantify the instrumental broadening contribution. The chemical composition of the powders was checked by using an energy dispersive spectrometer (EDX) mounted on a JEOL-JSM 6100 scanning electron microscope (SEM) working at 35 kV. FTIR spectra of the as-produced particles (before carbon coating) were recorded with a Bruker Equinos spectrometer using the KBr pellet technique. They were obtained between 400 and 4000 cm$^{-1}$ for 50 scans and a resolution of 4 cm$^{-1}$. Raman scattering (RS) spectra were recorded on a Jobin-Yvon U1000 double monochromator using the 514.5 nm line from a Spectra-Physics 2020 argon–ion laser. Standard photon-counting techniques were used for detection. In a typical spectral acquisition, three RS spectra, each recorded with a resolution of 2 cm$^{-1}$, were averaged. Care was taken against sample photo-degradation using a low excitation power of 10 mW. Thermal analyses were performed with a Thermo Gravimetry/Differential Thermal Analyzer (TG/DTA) Setaram TGA92 apparatus from room temperature up to 700 °C in air or H$_2$/N$_2$ at a heating rate of 20 °C min$^{-1}$. The magnetic properties of the produced powders were carried out on a Quantum Design MPMS-5S SQUID magne-tometer. The thermal variation of the dc-susceptibility of each sample is measured from 300 to 4 K using an applied magnetic field of 2 kOe. The isothermal magnetization was also measured as a function of the magnetic field up to 50 kOe. All the measurements were performed on the as-prepared powders slightly compacted in a plastic sampling tube, in order to prevent the particles from moving during the experiments. The size and shape of the prepared particles were analyzed on a JEOL-100-CX II transmission electron microscope (TEM) operating at 100 kV.

### 2.5. Electrochemical investigation

Electrochemical testing of the LiFePO$_4$ cathode materials was performed using screw-type cells with a lithium metal anode. The cathode materials were made by mixing 84% of active materials with 3% of carbon black and 3% of very gross carbon fiber (VGCF) and 10% of polyvinylidene fluoride (PVDF). The resulting paste was coated onto an aluminum mesh. The electrolyte was a solution of 1 mol L$^{-1}$ LiPF$_6$ in a mixture of ethylene carbonate (EC) and dimethyl carbonate (DMC); (v/v; 1:1). The cells were cycled over the voltage range of 2.0–4.0 V.

## 3. Results

### 3.1. Phase analysis

The phase purity of the as-prepared LiFePO$_4$ powders was determined by XRD. Fig. 1 shows the recorded patterns. All the diffraction peaks are perfectly indexed in the orthorhombic olivine structure (space group *Pnma*), except in the case of the sample produced in DEG. The powders produced in TEG and tEG exhibit a high crystalline quality when compared to those produced in
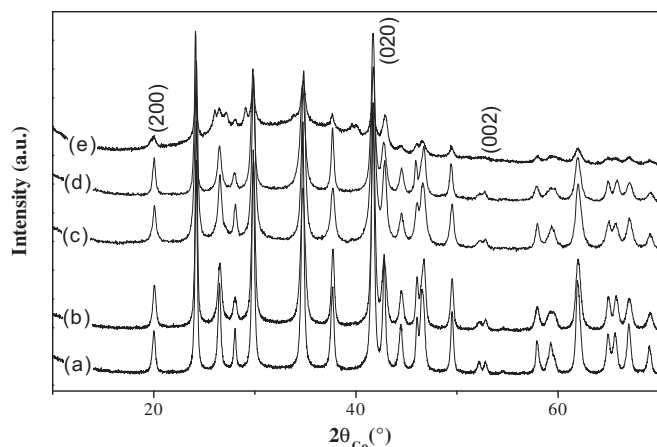
**Fig. 1.** XRD pattern of the as-produced LiFePO$_4$ powder in TEG solvent (samples a, b), tEG solvent (samples c, d) and DEG solvent (sample e). All the peaks are intrinsic. For clarity, we have labeled only the peaks corresponding to the directions in which the coherence lengths have been reported in Table 2.

DEG, with refined cell parameters (Table 1) in agreement with those of the stoichiometric bulk phase ($a = 10.3470$ Å, $b = 6.0189$ Å and $c = 4.7039$ Å) [16]. In DEG, however, an important amorphous contribution is detected. TEG and tEG have a boiling temperature of 325 and 285 °C, respectively, while that of DEG does not exceed 245 °C. Clearly, the solvents with high boiling temperatures promote the formation of highly crystallized olivine phase, since the reaction occurred at higher temperatures. Therefore, we will now on focus our study on the powers produced in TEG and tEG only. Note that in these solvents, under the adopted synthesis conditions, a reaction time of 4 h appears to be enough to produce particles with high crystalline quality, compared to the 16 and 20 h required in previous works using the polyol process. The volume $V$ of the unit cell is also reported in Table 1, since the value of this parameter is a probe of the presence of antisites (Fe on Li site) that limit the diffusivity of Li in LiFePO$_4$ and thus damage the electrochemical performance [17,18]. A sample free of antisites should have a lattice parameter in the range 290–291 Å$^3$ [17,19]. The value of $V$ falls in this range for all the samples except the sample (c). For this sample, $V = 291.15(5)$ Å$^3$, which, after the Fig. 3 in Ref. [17] corresponds to a concentration of antisite defects the order of 3%.
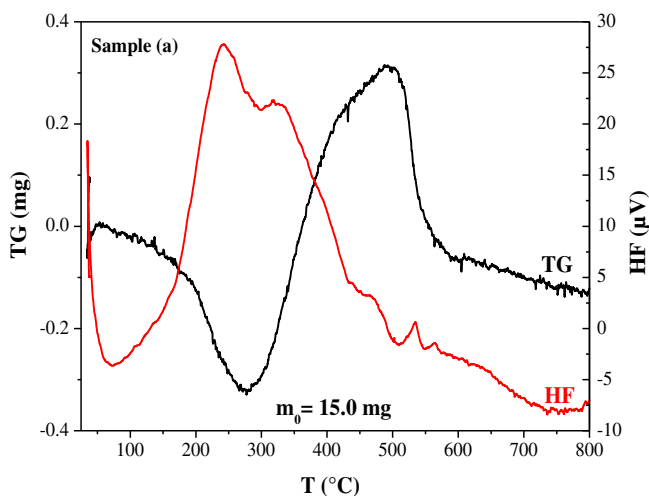


**Fig. 2.** Thermogravimetry (TG) and HF plot of the as-produced sample a.

EDX analysis confirmed the formation of the desired olivine phase. According to the LiFePO$_4$ composition, equal amounts of Fe and P atoms are found as expected. All the samples contained a small amount of carbon at the surface of the particles. Such contamination was already detected in polyol-made inorganic (metal or oxide) particles and attributed to residual acetate and/or polyol molecules adsorbed at the surface of the particles [20–23]. Usually such molecules act as a protective layer avoiding dramatic surface oxidation. The amount of mineral (water) and organic (polyol) adsorbed species were measured by thermogravimetry analysis (TG) in air (Fig. 2). TG results showed departure of these components below 350 °C with a total weight loss of 6%, in two main steps: a first endothermic peak at about 100n °C attributed to the physisorbed water molecules and a second exothermic peak around 300 °C attributed to loss of the chemisorbed polyol species. At higher temperature LiFePO$_4$ oxidation occurred as revealed by the significant weight increase in the TG curve due to oxygen incorporation in the cell lattice [24].

### 3.2. Morphology analysis

The microstructure of the as-produced powders was inferred from both XRD peak broadening analysis and direct TEM observation. MAUD refinements allowed us to estimate the average size and shape of the coherent diffraction domains in all the produced powders. Both the crystallite size and shape concur in determining the broadening of the XRD peaks, so that the sample-related line shape can be considered as a convolution of strain- and size-related profiles. In the present case, to achieve satisfactory fits of the experimental diffraction profiles, it was necessary to employ anisotropic contributions to the peak-shape function. Indeed, the peak related to the $(0k0)$ direction appeared to be relatively broad. The remarkable anisotropy that characterizes the profile function of samples indicates either a larger number of defects in the $b$ direction and/or the anisotropic shape of the crystallites (coherent domains) that should be contracted along the crystallographic $b$-direction or reversely elongated along $a$- and $c$-directions. Strain- and size-related contributions are different functions of the diffraction angle [15]. To distinguish between the two effects, refinements showed that in all the studied powders the microstrain effect is negligible. The shape and the size of the crystallites deduced from these refinements clearly appeared to be anisotropic (Fig. 3) with an average thickness, width and length of few tens of nanometers, depending on the synthesis conditions: when the precursor concentration decreases, the length of the crystallites increases, while the width and thickness decrease. The coherence lengths $L$ along the three crystallographic axes are reported in Table 2 for the different samples. This evolution is even more pronounced when tetraethyleneglycol was replaced by triethyleneglycol. Such a change in morphology was also observed in the recorded TEM images on the as-produced samples (Fig. 4). The particles appeared to be nano-platelets more or less elongated, when their synthesis conditions were varied. All the platelets in a given sample have the same shape and the size distribution is reported in Fig. 5 for the samples (a) and (b) that we have selected to illustrate the effect of the dilution rate in the solvent during the synthesis process, as the TEG solvent used for these two samples gives better results in terms of electrochemical properties, as we shall see later. The average length $<L_{TEM}>$ and width $<L_{TEM}>$ of the particles deduced from the analysis of the TEM images are reported in Table 2 for all the samples. There is no evidence of any defect, dislocation, or amorphous layer in any of the samples. Nevertheless, the particles produced in TEG seemed to be better crystallized than the ones obtained in tEG. The high-resolution image of one representative particle of each sample shows fringes corresponding
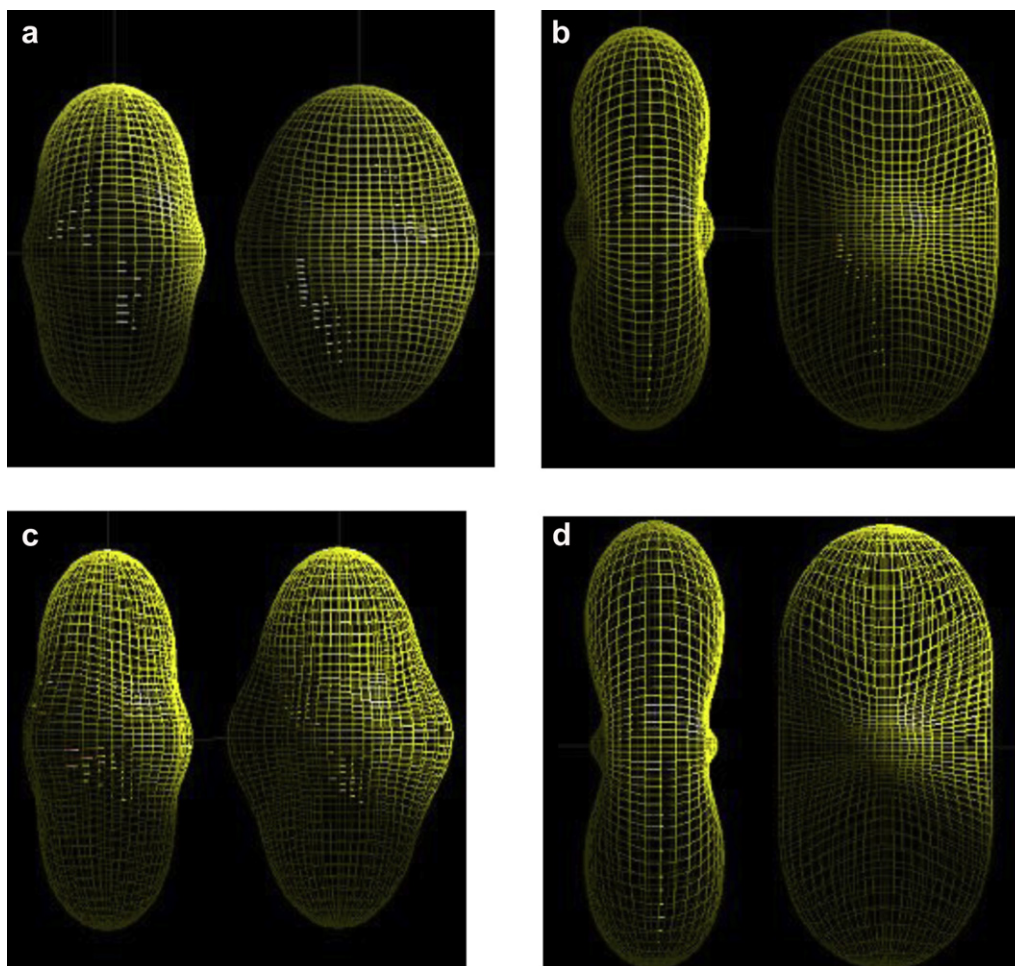
**Fig. 3.** The average shape of the crystallites for the samples a, b powders synthesized in TEG solvent, and the samples c, d synthesized in tEG solvent, as inferred from the analysis of the XRD pattern (Fig. 1), using the MAUD software.

to crystallographic planes of the orthorhombic lattice of the olivine structure. As mentioned in Section 2, the particles have to be carbon-coated before electrochemical measurements, and the heating at 700 °C in the process does not alter significantly the morphology of the particles [5]. This is confirmed by XRD performed on the resulting nanocomposites (not shown) after coating, and by TEM observation that also showed a uniform and homogenous 3-nm thick carbon coat (Fig. 6).

### 3.3. Physical characterization

Fig. 7 shows the FTIR spectrum of the as-produced powder, together with that of free polyol (TEG). The comparison between

**Table 2**
Average coherence lengths of the crystallites of the different powders labeled a–d according to Table 1. These lengths are noted $<L>$, with the axes labels in index. The lengths $<L_{TEM}>$ and width $<l_{TEM}>$ of the particles deduced from the analysis of the TEM images are also reported. The figure after the $\pm$ symbol is the half-width of the Gaussian that fits the size distribution.

| Sample | $<L_{200}>$ (nm) | $<L_{020}>$ (nm) | $<L_{002}>$ (nm) | $<L_{TEM}>$ (nm) | $<l_{TEM}>$ (nm) |
|---|---|---|---|---|---|
| (a) | 38.1 | 45.5 | 56.1 | 68 ± 20 | 26 ± 9 |
| (b) | 40.4 | 19.6 | 57.6 | 195 ± 32 | 37 ± 4 |
| (c) | 23.6 | 25.2 | 39.8 | 90 ± 15 | 40 ± 7 |
| (d) | 36.1 | 15.4 | 62.2 | 600 ± 96 | 39 ± 6 |

the two spectra gives evidence of the polyol adsorption, and the additional structures of the spectrum of the LiFePO$_4$ particles spectrum give evidence of the formation of the olivine phase. The main feature is the appearance of intra-molecular symmetric and antisymmetric O–P–O bending and P–O stretching bands at 372–647 cm$^{-1}$ and 945–1139 cm$^{-1}$, respectively, related to the (PO$_4$)$^{3-}$ group in the LiFePO$_4$ phase [25]. The H–O–H bending band related to adsorbed water and C–H and O–H stretching bands related to the adsorbed alcohol occurs at 1620 cm$^{-1}$ and 2800 and 3500 cm$^{-1}$, respectively [26]. It must be noticed that some vibrational features related to the (PO$_4$)$^{3-}$ group in Li$_3$PO$_4$ (typically at 424 cm$^{-1}$) and LiFeP$_2$O$_7$ (at 762 and 1180 cm$^{-1}$) phases are not detected [27]. Raman spectra of the as-produced particles were also recorded and compared to that of free polyol (TEG). The results are consistent with the analysis of the FTIR spectra: the strong peak at 945 cm$^{-1}$ and very weak lines between 1358 and 1590 cm$^{-1}$ are related to the PO$_4^{3-}$ anion stretching vibration in the LiFePO$_4$ crystals and to the residual carbon-based contamination (mainly adsorbed polyol) vibration, respectively (Fig. 8) [28]. Note, however that the TEG-related lines coming from TEG residues are very weak, and have comparable intensities for all the samples. The RS spectroscopy is a probe of the surface of the samples since the spectra are detected by reflectivity measurements, while the FTIR spectra are recorded by transmission measurements exploring the bulk of the material. Therefore, the fact that the TEG-related lines in Fig. 8 are so small gives evidence that the surface covered by the TEG
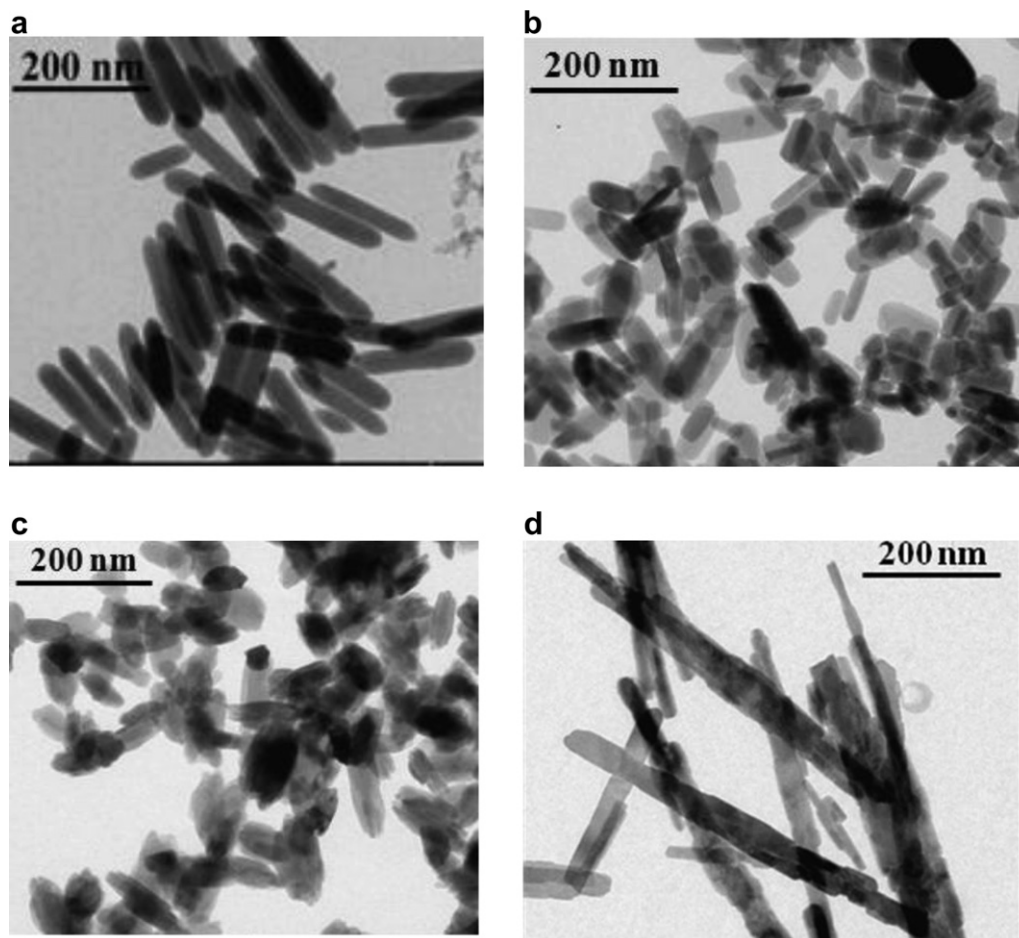
**Fig. 4.** TEM images of an assembly of LiFePO$_4$ particles constituting the as-produced LiFePO$_4$ powders synthesized in TEG solvent (samples a, b), and tEG solvent (samples c, d).
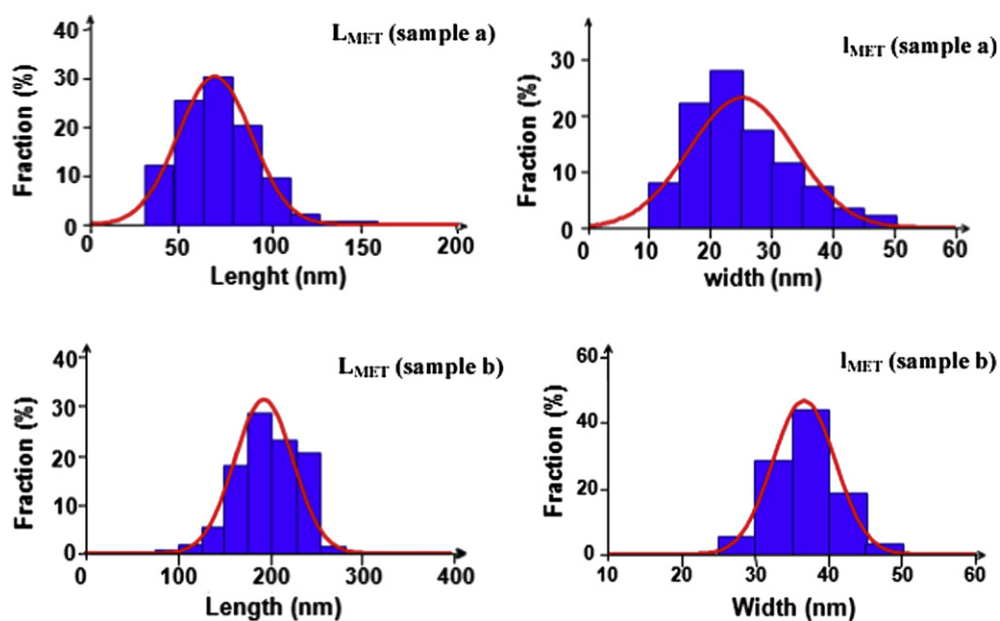


**Fig. 5.** Size (length and width) distributions of the particles constituting the sample a, b synthesized in TEG solvent, as deduced from the analysis of TEM images. The fit of the distribution by a Gaussian is also reported. The average sized and half width of the Gaussian distributions for all the samples can be found in Table 2.
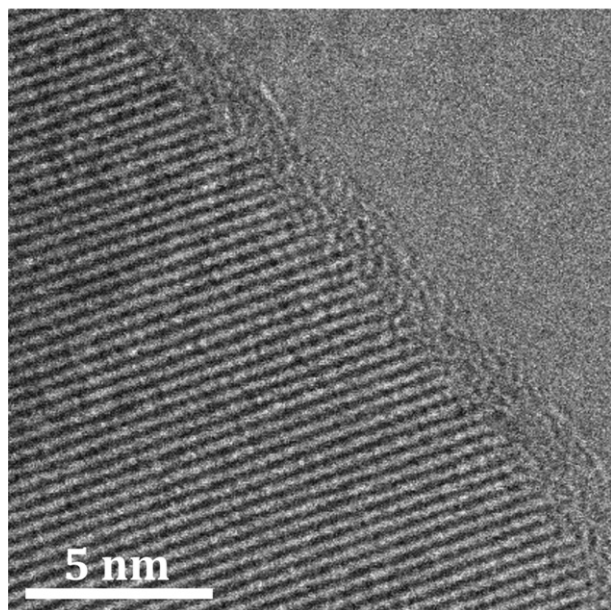
Fig. 6. High-resolution TEM image of a LiFePO$_4$ (sample a) illustrating the 3-nm thick amorphous conductive carbon coat.

residues is actually small. We shall return to this important result in next section in the framework on the discussion on the electrochemical properties.

Magnetic measurements were performed on the as-produced powders, since they are very sensitive to characterize the purity of the samples [29]. Any Fe$^{2+}$ oxidation and ferromagnetic trivalent iron oxide should be clearly evidenced in the thermal variation of the dc-magnetic susceptibility and the isothermal variation of the magnetization as a function of field. The magnetization curves $M(H)$ (not shown) are linear for all the samples at all temperatures $T > 10$ K, so that none of the ferro- or ferrimagnetic impurities that may poison the material is present in our case [29]. The thermal variation of the reciprocal magnetic susceptibility $\chi_{\mathrm{m}}^{-1}$ (Fig. 9) is in quantitative agreement with prior works. At high temperature, the variation of $\chi_{\mathrm{m}}^{-1}(T)$ obeys the Curie–Weiss law. The value of the effective magnetic moment of Fe$^{2+}$ deduced from the fit of the experimental data by the Curie–Weiss law in the 100–310 K range
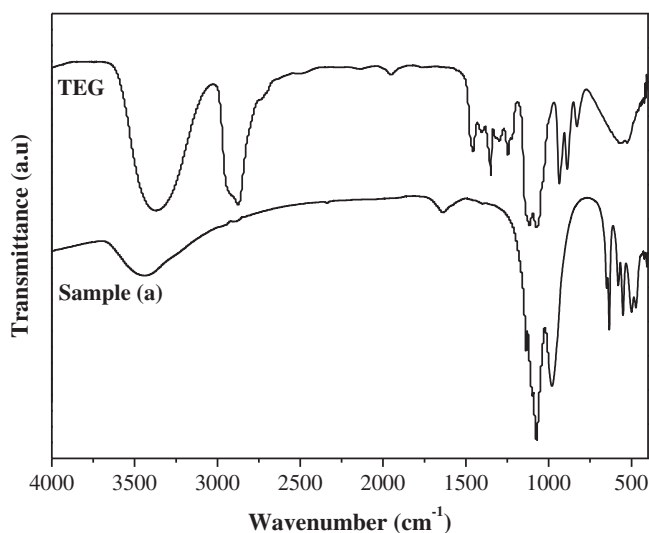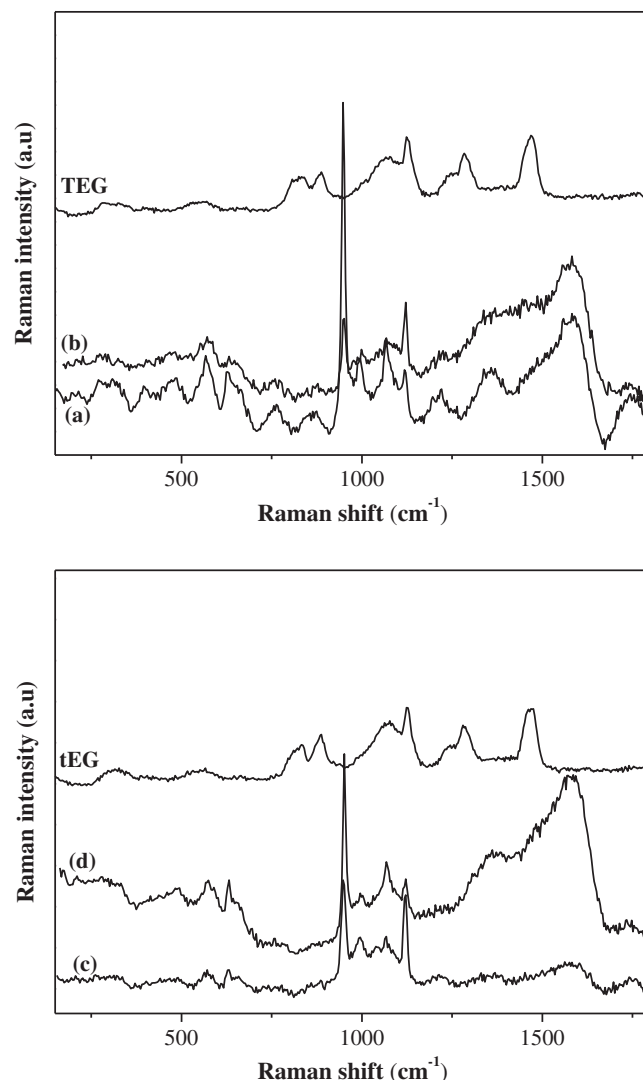




Fig. 8. Raman spectrum of the samples synthesized in TEG solvent (samples a, b), and tEG solvent (samples c, d).

is $\mu_{\mathrm{eff}} = 5.3 \pm 0.1 \mu_{\mathrm{B}}$ for all the samples (a)–(d), slightly higher that that of the spin only ($S = 2$) free Fe$^{2+}$value in the high spin state ($4.9\mu_{\mathrm{B}}$), and in agreement with the prior results on this material, because of the polarons associated to a small ($<1\%$) concentration of Li-vacancies [30] and/or because of the contribution of Fe$^{3+}$ ions in the surface layer [31]. The shift of the curves in Fig. 9 is reminiscent of the shift of $\chi_{\mathrm{m}}^{-1}$ observed in single crystals oriented along the different orientations parallel and perpendicular to the *c*-axis of the lattice [32]. This effect is linked to the anisotropic shape of the powders. When the particles are spherical, the orientations of the *b*-axis of the crystallites with respect to the magnetic field are randomly distributed, so that the magnetic susceptibility is just an average on the different components: $\chi_{\mathrm{m}} = (\chi_{\|} + \chi_{\perp,a} + \chi_{\perp,c})/3$ in obvious notations. In the present case, however, the shape of the particles is not spherical and the steric effect implies that their orientations with respect to the field are not random, but out of control, depending on how the powder has been prepared in the container used in the magnetic measurements. The anisotropy does not affect significantly $\mu_{\mathrm{eff}}$, but there is a difference of 55% in the values of the paramagnetic Curie temperature between the cases $H\|b$ and $H\|c$ so that this parameter is very sensitive to the orientation of the crystallites [32]. This effect observed in Fig. 9 is thus



Fig. 7. FTIR spectra of the samples synthesized in TEG solvent (sample a). The FTIR spectrum of TEG is also reported, for comparison.
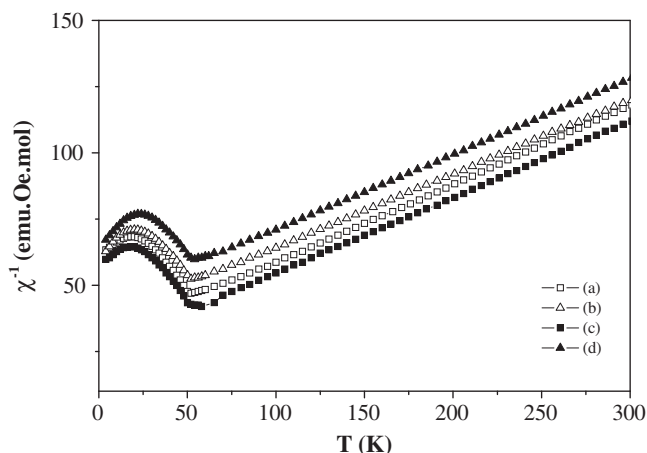
**Fig. 9.** Thermal variation of the inverse of the magnetic susceptibility of the samples synthesized in TEG solvent (samples a, b), and tEG solvent (samples c, d).

the consequence of the fact that the particles are well crystallized in an anisotropic shape. At low temperature, the cusp of $\chi_m^{-1}(T)$ curve is observed at the Néel temperature $T_N = 50$ K [33].

### 3.4. Electrochemical analysis

Fig. 10 shows the voltage profile at C/24 rate for the cells built with all the C-LiFePO$_4$ composite samples as the active cathode elements in the voltage range of 2.5–4.0 V. The cells showed huge differences in the capacity between the different samples, ranging from 151 to 65 mAh g$^{-1}$ when the starting LiFePO$_4$ particles were changed from sample (a) to sample (d), respectively. In all the cases a well-formed plateau at ca. 3.45 V was observed. Except for sample

(a), which gave results comparable to the best results reported for C-LiFePO$_4$ reported in the literature, the measured capacities are smaller, despite the LiFePO$_4$ size reduction and the conductive carbon coating.

## 4. Discussion

To tentatively understand what happened in the present systems, we performed RS spectroscopy study on the as-produced particles after a subsequent heating at 700 °C under reductive atmosphere (H$_2$/N$_2$ 4%) to mimic the carbon coating treatment, but without the lactose carbon source, aiming to determine the eventual role of the residual adsorbed polyol species. Polyol molecules have often been used as carbon source in coating process [34–36]. For example, Yang et al. synthesized LiFePO$_4$ powders by a sol-gel route using ethyleneglycol (EG) as solvent. Annealing the dried initial gels at temperature in the range 500–700 °C under inert atmosphere for several hours results in the formation of LiFePO$_4$ coated with an homogeneous in-situ carbon layer of a few weight percent (less than 2 wt.-%), which takes its origin from adsorbed solvent molecules [34,35]. Recorded Raman spectra on all the polyol-made LiFePO$_4$ powders after heating at 700 °C gives evidence of the same effect. Indeed, the annealed powders presented two bands at 1358 and 1590 cm$^{-1}$ corresponding to D- and G-carbon bands, respectively, in addition to the band at 945 cm$^{-1}$ (Fig. 11) characteristics of the LiFePO$_4$ bulk below the carbon layer. The peak intensity ratio of these two bands, ($I_D/I_G$) as well the G-band position give a measure of the quality of the carbon coating, smaller $I_D/I_G$ indicating more conductive structure (predominantly $sp^2$ bonding) [37,38]. The position of the G-band shifts downwards to 1500 cm$^{-1}$ for amorphous carbon, when a loss of aromatic bonding appears. To resolve the contribution of the residual carbon coating in the recorded Raman spectra, we applied a standard peak
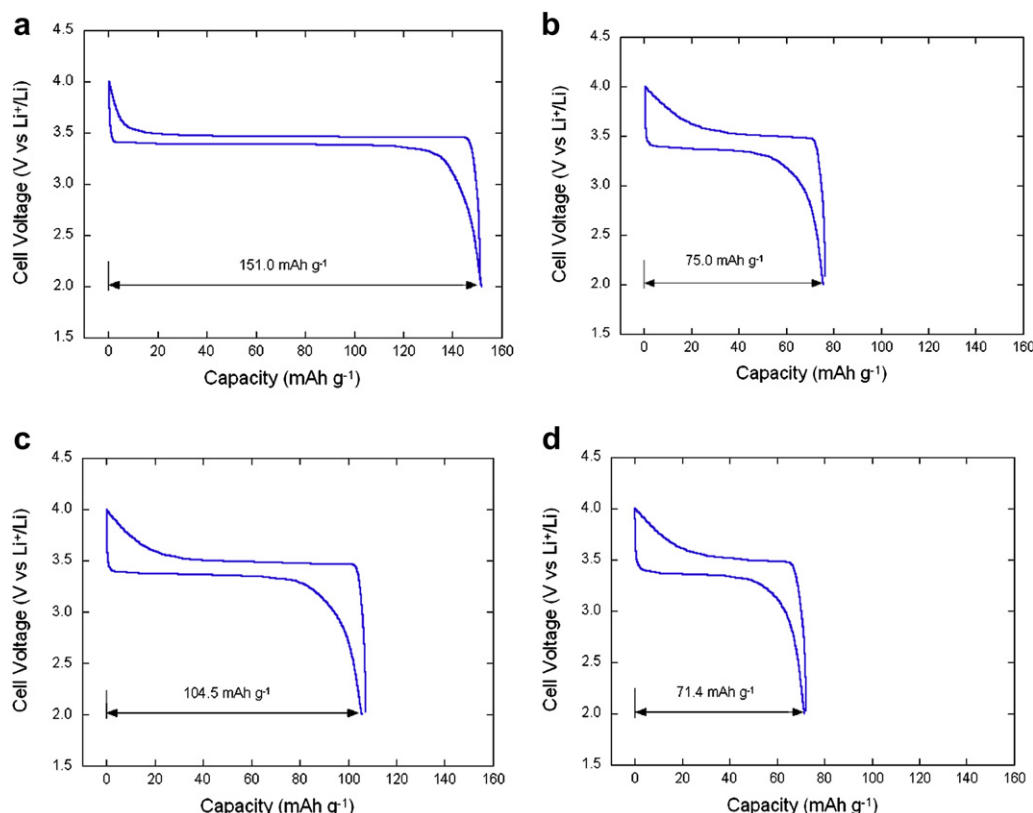


**Fig. 10.** Charge–discharge profiles of the samples (a)–(d) measured at C/24 rate.
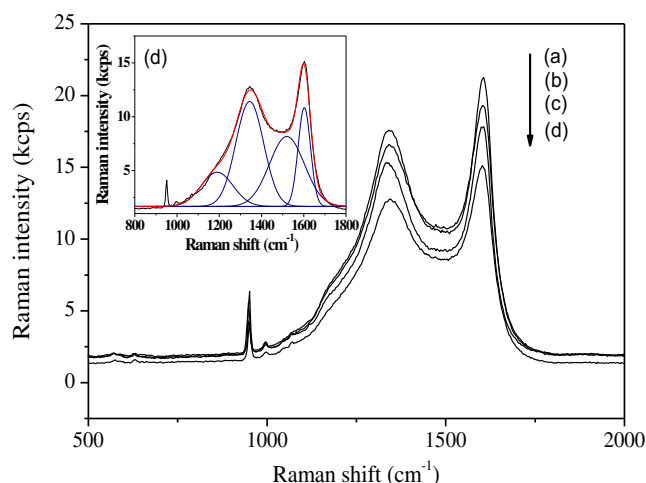
**Fig. 11.** Raman spectra of LiFePO$_4$ obtained after decomposition at 700 °C of polyol adsorbed at the surface of the particles produced in TEG solvent (samples a, b), and tEG solvent (samples c, d). The bands associated to the carbon due to this decomposition in the range 800–1800 cm$^{-1}$ were resolved using four Gaussian profiles; an illustration of this deconvolution is given in insert.

deconvolution procedure (see the inset in Fig. 11). A deconvolution using only two carbon D and G lines did not give accurate results. Like in prior works on the carbon coat of LiFePO$_4$ four Gaussian bands were needed to account for the observed Raman features with minimum error [38]. Those bands are situated at ∼ 1190, 1350, 1518 and 1590 cm$^{-1}$. The D and G bands are those located at 1350 and 1590 cm$^{-1}$, respectively [38]. The intensity of these two bands $I_D$ and $I_G$ is defined as the integral of these two Gaussians, respectively.

The three samples (b), (c), (d) have the same ratio $I_D/I_G = 2.37 \pm 0.01$ within uncertainty. On another hand, sample (a) has a smaller ratio $I_D/I_G = 2.31$. This is actually much larger than the value ∼ 1.4 obtained for the carbon coat of bare LiFePO$_4$ particles by the lactose or a similar route [39], so that the carbon associated to the polyol residues is clearly not conducting. Note the sample (a) that has the best capacity according to Fig. 10 is also the sample for which the carbon coat is more conductive. However, it should be pointed out that he value of $I_D/I_G$ for this sample (a) differs from that of the other samples by less than 3%, which is marginal and cannot explain the difference by a factor two of the capacity between this sample (a) and the samples (b) or (d). In addition, the samples (c) and (d) that have roughly the same ratio $I_D/I_G$ also differ in capacity by a factor two, so that the difference in the conductivity of the carbon deposited on the surface of the different particles by the residues of polyol between the samples is not the pertinent parameter that is responsible for such a disparity in the electrochemical performances. We can then simply retain from this experiment that the polyol remaining at the surface of the LiFePO$_4$ is a carbon precursor, as it generates carbon evidenced by the characteristic Raman lines associated with it. The analysis of the Raman spectra has shown that this carbon is rather insulating, even after heating at 700 °C.

The insulating nature of the polyol residue is not surprising, because graphitic carbon requires heating at much higher temperatures. We have already noticed in earlier works that the formation of a layer of conductive carbon at temperature as low as 700 °C with lactose was unexpected, and requires some catalytic effect of the iron with carbon at the surface of LiFePO$_4$ [40]. This catalytic effect, however, is possible only in case the surface of the particles is clean. The adsorbed polyol species transforms under reducing atmosphere in a non-conductive deposit on the LiFePO$_4$ particles, creating an insulating barrier that opposes the electron

transfer. This layer prevents the direct contact of the LiFePO$_4$ surface with the carbon issuing from the lactose, and this catalytic effect is lost. Let us investigate the importance of the damage on the electrochemical properties induced by this polyol residue. The large value of the capacity for the samples (a) and (c) implies that the polyol residue covers only a small part of the surface of the particles, and does not prevent the conductive carbon layer deposited by the lactose route from percolating through the structure. This is actually consistent with the analysis of the Raman spectra in Fig. 8 according to which the surface covered by the polyol residues is very small. For the samples (b) and (d), which were prepared with a concentration of polyol ten times larger, the polyol residue might cover a larger portion of surface of the particles than for samples (a) and (c), in which case the capacity (b) and (d) should be reduced. This is indeed confirmed in Fig. 10. In this spirit, the dramatic decrease of the capacity of samples (b) and (d) might be due to the fact that the polyol residues cover a large portion of the surface of these particles, preventing any efficient coating of LiFePO$_4$ by conductive carbon by the lactose process. Indeed, we know from our prior works that the conductive carbon layer is mandatory to obtain good electrochemical properties irrespective of the size of the particles [5]. Nevertheless, the attribution of the poor capacity of the samples (b) and (d) to the polyol residue is ruled out by the analysis of the Raman spectra in Fig. 11, because the integrated intensity of the Raman bands associated to the insulating carbon due to the polyol residues is actually smaller in samples (b) and (d) than in samples (a) and (c), respectively, so that the amount of carbon deposited is smaller.

Another parameter plays the key role, namely the coherence length along the *b*-direction, since it is the axis of the Li channels through which the Li$^+$ ions move in the insertion/de-insertion process. We have reported in Fig. 12 the capacity of the samples as a function of the coherence length $<L_{020}>$ along this axis. The correlation is obvious: the longer $<L_{020}>$, the larger the capacity is. This figure also illustrates the importance played by another synthesis parameter, namely the choice of the solvent that impacts the crystallinity of the samples. The choice of a solvent with larger boiling temperature $T_b$ is benefit to the crystallinity: DEG ($T_b = 245$ °C) fails to synthesize crystallites, tEG ($T_b = 285$ °C) leads to the formation of crystallites, but still with a concentration of 3%
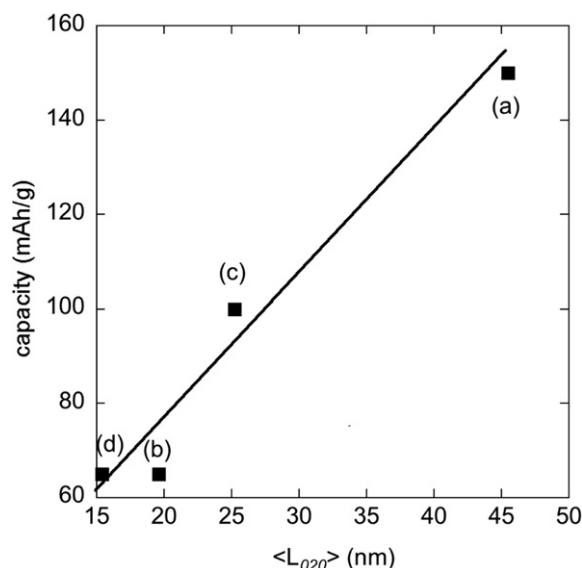


**Fig. 12.** Capacity of the C-LiFePO$_4$ samples as a function of the coherent length of their crystallites along the (010) axis. The letters refer to the samples (a)–(d).

of iron on Li sites known to reduce the capacity. This defect linked to the decrease of $<L_{020}>$ is responsible for the difference of capacity between the samples (a) and (c). TEG ($T_b = 315\,°C$) has finally the boiling temperature sufficient to synthesize samples with good crystallinity and free of the antisite defects, so that the capacity at low C-rate is 151 mAh g$^{-1}$. This is actually close to the theoretical value if we take into account that the capacity of the cheap cells prepared in the laboratory are about 10 mAh g$^{-1}$ smaller than the results measured with a more elaborate '18650'-type cell, as shown in [39]. This result corroborates the good performance of samples obtained recently by using TEG [40]. Note that in the hydrothermal synthesis process, the same effect is also observed, but shifted in temperature: samples with a good crystallinity are synthesized if the temperature is larger than 200 °C, but lowering the synthesis temperature below this value results in increasing concentration of antisite defects [41–43]. Therefore, the synthesis by polyol process requires a synthesis temperature $T_S > 300\,°C$, intermediate between the hydrothermal process that requires $T_S > 200\,°C$, and the solid-state reaction that requires $T_S > 400\,°C$ [44].

Note also that earlier works using polyol process only considered the XRD patterns as the unique proof of the phase formation, and neglect the fact that the detectionlimit of this technique is about 4–5 at.%. It means some percent of crystalline impurities, particularly iron-based nanocrystalline ones, have not been detected, and actually, we met this problem in a first attempt to prepare the samples using the same synthesis parameters previously published. This is another reason for the broad differences in electrochemical performance published so far using this synthesis process. Indeed, the quality control of the samples requires the combination of XRD, optical and magnetic measurements [45].

## 5. Conclusion

Size-tuned LiFePO$_4$ nanoplatelets were successfully prepared using polyol process, varying the synthesis conditions, namely the solvent nature and the metal precursor concentration. FTIR and Raman spectra evidenced the presence of residual polyol species at their surface. These species lead to non-conductive carbon deposit at the surface of the particles, that remain during the carbon coating treatment involving lactose pyrolysis at 700 °C under inert atmosphere. However, the part of the surface of the particles occupied these polyol residues is too small to prevent the conductive carbon layer deposited by the lactose root from percolating in the structure so that the electrochemical properties are governed by two parameters that determine the crystallinity of the as-produced particles:

- The concentration of the iron salt in the solvent: this concentration should be large enough to avoid the formation of defects, in particular Fe on Li-sited that reduce the diffusivity of Li and the coherence length along the (010) axis.
- The nature of the solvent: the solvent must have a high boiling temperature (>300 °C) to obtain well-crystallized sample.

We have found that the TEG solvent with iron precursor concentration $1.725 \times 10^{-2}$ mol L$^{-1}$ leads to an optimized product, made of particles about 10-nm thick, well crystallized, free of impurity, with a capacity of 151 mAh g$^{-1}$ at low C-rate.

## References

[1] A.K. Pahdi, K.S. Nanjundaswamy, J.B. Goodenough, Journal of Electrochemical Society 144 (1997) 1188–1194.

[2] C.Y. Ouyang, S.Q. Shi, Z.X. Wang, X.J. Huang, L.Q. Chen, Physical Review B 69 (2004) 104303–104307.
[3] P.P. Prosini, M. Lisi, D. Zane, M. Pasquali, Solid State Ionics 148 (2002) 45–51.
[4] N. Ravet, Y. Chouinard, J.F. Magnan, S. Besner, M. Gauthier, M. Armand, Journal of Power Sources 97 (2001) 503–507.
[5] C.M. Julien, A. Mauger, K. Zaghib, Journal of Materials Chemistry 21 (2011) 9955–9968.
[6] K. Zaghib, P. Charest, M. Dontigny, A. Guerfi, M. Lagacé, A. Mauger, M. Kopek, C.M. Julien, Journal of Power Sources 195 (2010) 8280–8288.
[7] M.S. Islam, M.S.D.J. Driscoll, C.A.J. Fisher, P.R. Slater, Chemistry of Materials 17 (2005) 5085–5092.
[8] D. Morgan, A. Van der Ven, G. Ceder, Electrochemical and Solid-State Letters 7 (2004) A30–A32.
[9] S. Nishimura, G. Kobayashi, R. Ohoyama, R. Kanno, M. Yashima, A. Yamada, Nature Materials 7 (2008) 707–711.
[10] G. Chen, X. Song, T.J. Richardson, Electrochemical and Solid-State Letters 9 (2006) A295–A298.
[11] D.H. Kim, J.S. Im, J.W. Kang, H.Y. Ahn, J. Kim, Journal of Nanoscience and Nanotechnology 7 (2007) 3949–3953.
[12] D.H. Kim, T.R. Kim, J.S. Im, J.W. Kang, J. Kim, Journal of Physica Scripta T129 (2007) 31–34.
[13] T.R. Kim, D.H. Kim, H.W. Ryu, J.H. Moon, J.H. Lee, S. Boo, J. Kim, Journal of Physics and Chemistry of Solids 68 (2007) 1203–1206.
[14] S.P. Badi, M. Wagemaker, B.L. Ellis, D.P. Singh, W.J.H. Borghols, W.H. Kan, D.H. Ryan, F.M. Mulder, L.F. Nazar, Journal of Materials Chemistry 21 (2011) 10085–10093.
[15] L. Lutterotti, S. Matthies, H.R. Wenk, IUCr: Newsletter of The Commission on Powder Diffraction 21 (1999) 14–15.
[16] V.A. Streltsov, E.L. Belokoneva, V.G. Tsirelson, N.K. Hansen, Acta Crystallography B49 (1993) 147–153.
[17] P. Axmann, C. Stinner, M. Wohlfahrt-Mehrens, A. Mauger, F. Gendron, C.M. Julien, Chemistry of Materials 21 (2009) 1636–1644.
[18] G.K.P. Dathar, D. Sheppard, K.J. Stevenson, G. Henkelman, Chemistry of Materials 23 (2011) 4032–4037.
[19] P. Jozwiak, J. Garbarczyk, F. Gendron, A. Mauger, C.M. Julien, Journal of Non-Crystal Solids 354 (2008) 1915–1925.
[20] R. Boubekri, Z. Beji, K. Elkabous, G. Viau, S. Ammar, F. Fiévet, H.J. von Bardeleben, A. Mauger, Chemistry of Materials 21 (2009) 843–855.
[21] S. Ammar, A. Helfen, N. Jouini, F. Fiévet, I. Rosenman, F. Villain, P. Molinié, M. Danot, Journal of Materials Chemistry 11 (2001) 186–192.
[22] G. Viau, F. Fievet-Vincent, F. Fievet, Journal of Materials Chemistry 6 (1996) 1047–1053.
[23] L. Poul, S. Ammar, N. Jouini, F. Fiévet, F. Villain, Solid State Sciences 3 (2001) 31–42.
[24] J.Z. Wang, S.L. Chou, J. Chen, S.Y. Chew, G.X. Wang, K. Konstantinov, J. Wu, S.X. Dou, H.K. Liu, Electrochemistry Communications 10 (2008) 1781–1784.
[25] C.M. Burba, R. Frech, Journal of Electrochemical Society 151 (2004) A1032–A1038.
[26] L. Poul, N. Jouini, F. Fiévet, Chemistry of Materials 2 (2000) 3123–3132.
[27] K. Zaghib, N. Ravet, M. Gauthier, F. Gendron, A. Mauger, J.B. Goodenough, C.M. Julien, Journal of Power Sources 163 (2006) 560–566.
[28] M.S. Bhuvaneswari, N.N. Bramnik, D. Ensling, H. Ehrenberg, W. Jaegermann, Journal of Power Sources 180 (2008) 553–560.
[29] A. Ait Salah, A. Mauger, C.M. Julien, F. Gendron, Materials Science and Engineering B 129 (2006) 232–244.
[30] K. Zaghib, A. Mauger, J. Goodenough, F. Gendron, C.M. Julien, Chemistry of Materials 19 (2007) 3740–3747.
[31] K. Zaghib, M. Kopek, A. Mauger, F. Gendron, C.M. Julien, Journal of Power Sources 185 (2008) 698–710.
[32] G. Liang, K. Park, J. Li, R.E. Benson, D. Vaknin, J.T. Markert, M.C. Croft, Physical Reviews B 77 (2008) 064414–064425.
[33] R.P. Santoro, R.E. Newnham, Acta Crystallography 22 (1967) 344–347.
[34] J. Yang, J.J. Xu, Electrochemical and Solid-State Letters 7 (2004) A515–A518.
[35] J. Yang, J.J. Xu, Journal of Electrochemical Society 153 (2006) A716–A723.
[36] Y. Lin, M.X. Gao, D. Zhu, Y.F. Liu, G.H. Pan, Journal of Power Sources 184 (2008) 444–448.
[37] J.D. Wilcox, M.M. Doeff, M. Marcinek, R. Kostecki, Journal of Electrochemical Society 154 (2007) A389–A395.
[38] C.M. Julien, K. Zaghib, A. Mauger, M. Massot, Ait-Salah, M. Selmane, F. Gendron, Journal of Applied Physics 100 (2006) 63,511–63,517.
[39] K. Zaghib, M. Dontigny, A. Guerfy, P. Charest, I. Rodrigues, A. Mauger, C.M. Julien, Journal of Power Sources 196 (2011) 3949.
[40] N.N. Sinha, N. Munichandraiah, Journal of Electrochemical Society 7 (2010) A824–A829.
[41] J. Chen, M.S. Whittingham, Electrochemistry Communications 8 (2006) 855–858.
[42] J. Chen, M.J. Vacchio, S. Wang, N. Chernova, P. Zavajil, M.S. Whittingham, Solid State Ionics 178 (2008) 1676–1693.
[43] F. Brochu, A. Guerfi, K. Zaghib, M. Kopeć, A. Mauger, C.M. Julien, Journal of Power Sources, in press.
[44] N. Ravet, M. Gauthier, K. Zaghib, A. Mauger, J. Goodeough, F. Gendron, C. Julien, Chemistry of Materials 19 (2007) 2595–2602.
[45] K. Zaghib, A. Mauger, C.M. Julien, Journal of Solid-State Electrochemistry 16 (2012) 835–845.